TOOLCHAIN FOR FREE FLIGHT MEASUREMENT AND CODE VALIDATION PURPOSES
Test and Evaluation session

Benjamin M. Kutz, Manuel Keßler and Ewald Krämer
kutz@iag.uni-stuttgart.de, University of Stuttgart, IAG, Pfaffenwaldring 21, Stuttgart, 70569, Germany

Abstract

During the development of new numerical methods or in the validation process of a computational tool for a specific aerodynamic phenomenon, the comparison with experimental data is compulsory. Especially in helicopter aeromechanics, often experimental data is not available in the required depth or is very expensive to conduct. To overcome the lack of data the Institute of Aerodynamics and Gasdynamics (IAG) at the University of Stuttgart has developed a flying measurement platform. This model helicopter is able to collect the necessary flight test data on a model scale. These tests are embedded in a modular tool chain, which serves for validation purposes of the used fluid-structure coupling at IAG. In this tool chain the raw experimental data is obtained with the model helicopter and post-processed with a Kalman-filter. Numerical setups were built up to compute the structural dynamics and flight dynamics with the commercial comprehensive code CAMRAD II, and the fluid dynamics with the FLOWer flow solver. A coupling process assures that a free flight trim of the complete helicopter with elastic main rotor blades is computed. As an example, a free flight of the helicopter in ground proximity is regarded and results are shown.

NOMENCLATURE

α/AoA	angle of attack
β	sideslip angle
$\mathbf{\Phi}$	transition matrix
$\Delta\vec{x}$	deviation of the system state
$\Delta\vec{z}$	measurement deviation
$\hat{\vec{x}}$	system state
$\mathbf{B}$	external influence matrix
$\mathbf{G}$	noise matrix
$\mathbf{H}$	measurement matrix
$\mathbf{I}$	unity matrix
$\mathbf{K}$	Kalman gain matrix
$\mathbf{P}$	error-covariance matrix
$\mathbf{Q}$	noise-covariance matrix
$\mathbf{R}$	measurement noise matrix
μ	advance ratio
$\mu^\star$	normalised advance ratio
$\mathbf{\Omega}$	angular velocity
ϕ	helicopter roll angle
ψ	helicopter yaw angle
ρ	density
θ	helicopter pitch angle
Θ_0	collective setting of the main rotor
Θ_c	lateral cyclic
Θ_s	longitudinal cyclic
$\vec{F}$	trim loads vector
$\vec{f}(\vec{x})$	derived system state
$\vec{u}$	external influence vector
A	rotor disk area
c_T	thrust coefficient
F	force
h	height
M	moment
P	power
R	radius
v_∞	free stream velocity
9DOF	9 degree of freedom system
CFD	computational fluid dynamics
COTS	commercial off the shelf
DLR	german aerospace center
GCI	grid convergence index
GPS	global positioning system
IAG	Institute of Aerodynamics and Gasdynamics
IGE	in ground effect
Li-Po	lithium-polymer
MEMS	mircoelectromechanical systems
OGE	out of ground effect
RANS	Reynolds averaged Navier-Stokes
USR	ultra sonic range finder

1 INTRODUCTION

Often flight test data for specific aerodynamic phenomena or flight environments is not available and in any case very expensive to conduct with full scale helicopters. Especially ground effect measurements are seldom conducted with full helicopter configurations. Therefore, a severe lack of experimental data often hinders the validation of new computational models or the tackling of further flight situations.
At the Institute of Aerodynamics and Gasdynamics (IAG) of the University of Stuttgart, Fischer[1] developed a couple of years ago a flight test platform, which was recently extended and refurbished with modern measurement sensors and modern avionics. A computational modelling was set up to achieve the possibility to validate the computational fluid dynamics (CFD) code FLOWer from DLR[2] used at the institute. Both sides, the aerodynamics and the structural dynamics are modelled.

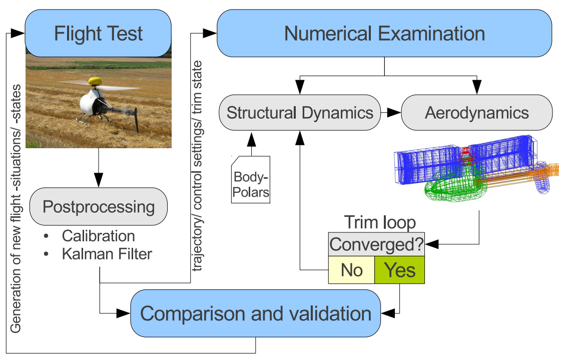

Fig. 1. Toolchain scheme

1.1 Tool chain

Figure 1 depicts the newly implemented toolchain at IAG. On the flight test side, data is collected for validation purposes. The specific test case is then computed in a trim iteration loop. The results are compared afterwards.
As the whole process is designed modular, models (e.g. a higher order approach in aerodynamics) can be exchanged or improved without any impact on the overall structure. This is especially helpful if validation of a new method or of a new flight case has to be achieved.
In this paper an overview of the new toolchain, the validation cycle and first results will be presented. Especially the build up and validation of all the parts of the chain will be addressed.

1.2 Motivation ground effect

The ground effect on the helicopter is characterised by an unsteady and extremely three dimensional behaviour of the flow. The forces and moments are altered significantly and show a much more distinct unsteady behaviour. Furthermore, the flow of the rotor interacts with the helicopter body and the ground, which often leads to recirculation phenomena. Due to its significance in the performance measures, the vibrations regarding fatigue and comfort as well as flight safety, the ground effect is a topic of interest since the beginning of helicopter flight.
Most studies in the past focused on the hover (Ref. 3) and forward flight (Refs. 4, 5) of model rotors in ground effect (IGE) and the comparison with results out of ground effect (OGE). At the beginning, theoretical (Refs. 6, 7, 8) and experimental (Ref. 9) correlations were derived. With those, the influence of the ground on the helicopter could be considered. Further experimental studies were done in Refs. 10, 11, 12, 13 and 14. The computational methods, which serve for the computation of the ground effect, are the finite state modeling (Ref. 15), the free vortex/ potential models (Refs. 16, 17, 18) as well as Euler-or Navier-Stokes code examinations (Refs. 19, 20, 21, 22, 23). Summaries were written in PhD theses (Refs. 24, 25 and 26).
At the IAG the ground effect was subject of several studies. Firstly, the ground influence on a fixed wing was simulated with the solver FLOWer (Ref. 27), then a model helicopter rotor in hover IGE (Ref. 28) was examined. This was then expanded towards forward flight (Ref. 29). For a validation with correct scale, Mach and Reynolds number, results of a comparison of an experimental and numerical approach with a complete helicopter in hover were analysed (Ref. 30).
In the present examination a trimmed complete helicopter IGE is examined experimentally and numerically with respect to the alignment of the body and the blade dynamics.

2 FLIGHT TEST

To obtain experimental free flight data a model helicopter is employed, which is equipped with different measurement sensors. The platform features the following sensors:

- Pitch-, lag-, flap-, azimuth-angle sensor at the main rotor
- Pitch-angle at the tail rotor
- GPS sensor

- Ultra sonic range finder (USR) for height above ground measurement
- pressure and temperature sensor
- 9 degree of freedom system (9DOF)
  - three accelerations
  - three angular velocities
  - three earth magnetic field axes
- JLOG2 system for performance measurements of the electric drive

These sensors are used to compose a trim target and a trajectory. This flight state is then computed afterwards.

2.1 Helicopter

The helicopter used is a Mikado LOGO 30 model helicopter with two blades for each rotor, main and tail alike. The steering is done via a $2.4GHz$ remote control system, and an additional flybarless system (BEASTX) supports the pilot for better situational awareness. The drive chain is powered by a Scorpion $3kW$ brushless motor, while Lithium-Polymer (Li-Po) accumulators provide the needed energy. A Jive controller from Kontronik steers the power flow. The weight of the overall system is about $5kg$.

Rotors

The rigid bar-less main rotor is equipped with symmetrical $0.62m$ blades, which leads to a radius of $0.7m$ featuring a NACA0013 like airfoil with a chord of $0.06m$. The angular velocity of the main rotor is $131rad/s$.
The tail rotor, which is attached in a pusher configuration, is equipped with two NACA0012 profiled blades with a radius of $0.1475m$, a chord of $0.026m$ and an angular velocity of $589rad/s$.

2.2 Measurement equipment

Hall-effect sensors The pitch, flap, lag and azimuth sensors of the main rotor and the pitch sensor of the tail rotor are Hall-effect-sensors, with a permanent magnet fixed to the blades. The great advantage is that there is no mechanical contact needed.

GPS sensor The GPS sensor receives and processes the signals of the visible GPS satellites and outputs the position, speed and GPS-height information.

USR sensor The USR sensor sends an ultra sonic pulse and measures the time until the reflected answer pulse is received. Out of the known speed of sound and the time between the emission and the receiving, the distance to the ground can be obtained.

MEMS sensors At the helicopter, also a sensor for the pressure/temperature and a 9 DOF board are attached. All those sensors are mircoelectromechanical systems (MEMS). They measure linear acceleration and angular velocities.

JLOG2 The last measurement system is the JLOG2 which is a COTS (commercial off the shelf) part. This data logger collects the data for e.g. the battery voltage, motor current, motor and rotor rotational rate. It also directly integrates the power consumption and logs several remote control settings (e.g. thrust setting).

Data logging devices At the helicopter three data logging devices are attached. The first is the already described JLOG2, the second system records the data of all the Hall-effect sensors and was developed at IAG, while the third is the COTS ”Logomatic V2” from SparkFun Electronics, which writes the data from the USR/ GPS/ 9DOF and pressure/temperature sensors onto a memory card. The time synchronisation between those three systems is established via the common logging of the start signal of the Hall-effect system. With this information a common time stamping is achieved.

2.3 Postprocessing

In a postprocessing step the measured data is read out of the several systems. Afterwards a Kalman filter is employed to compose the trajectory.

Kalman filter

To compute the trajectory of the flight path the final Kalman filter will use the data of the USR, GPS, 9DOF and pressure sensor. At the moment the usage of 9DOF, GPS and USR is implemented. In Ref. 31 the Kalman filter, which was developed specifically for this system, is described precisely, therefore, here only a short summary is given.

In Fig. 2 the implemented navigation-filter is depicted. Two loops are present:

- In the inertial strapdown algorithm, the high frequency data ($100Hz$) from the inertial measurement unit, that is, the accelerometer and the gyroscope, are used to compute the state and attitude of the helicopter. This is the basis of the system modelling. The system noise of this part is characterised by the noise of the inertial measurement unit sensors.
- The linearised Kalman-filter is the second loop, featuring a lower frequency (1Hz). As soon as data from the GPS, USR and magnetometer is available, these values will be compared with the

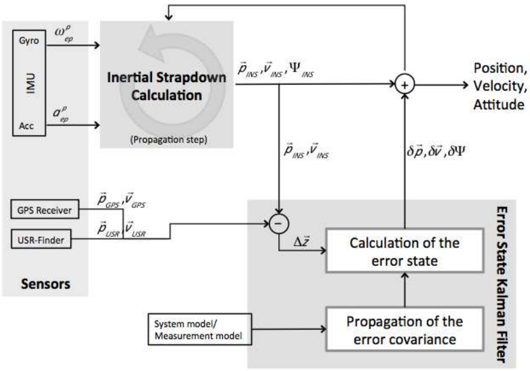

Fig. 2. Implemented inertial navigation system/GPS navigation-filter [32]

estimated system state from the first loop. The measurement deviations are regarded in the estimation loop and weighted with the Kalman gain matrix $\mathbf{K}$ to achieve a correction of the system state. The propagation and correction of the error-covariance matrix $\mathbf{P}$ is also done here. Normally the propagation of $\mathbf{P}$ should be done in the first loop, but to spare computational costs it is shifted towards the frequency of the second loop. Here $10Hz$ are selected, the correction is still done with $1Hz$.

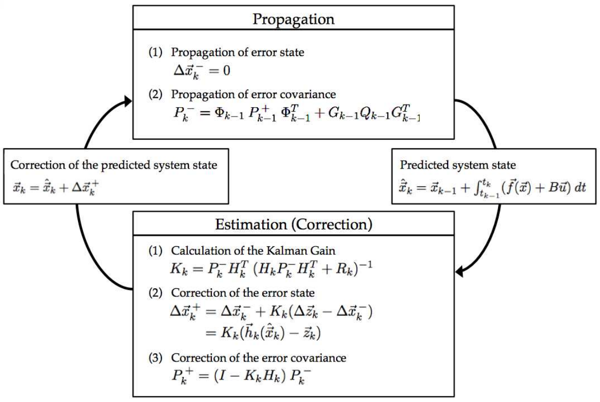

Fig. 3. Linearised Kalman-filter algorithm [32]

In general, the filter predicts in a propagation step (often also called prediction-step) the state of the system in the next timestep. Afterwards, the estimation step (often called update-step) corrects the previously found system state (Fig. 3). As the deviation from the estimated system state $\Delta\vec{x}$ is considered (error state formulation), the value is consequently zero in the propagation step (step (1) in Fig. 3). Then the error-covariance matrix $\mathbf{P}_k$ is propagated in (2). Here Φ_k is the transition matrix, defining the transition of the system state between the time steps, $\mathbf{Q}_k$ is the covariance matrix of the system noise and $\mathbf{G}_k$ is the noise transition matrix which is containing the system noise, e.g. uncertainties and inaccuracies in the modelling of the process. Then the assumed system state $\hat{\vec{x}}_k$ is determined with the previous system state $\vec{x}_{k-1}$ and the integral of the derived system state $\vec{f}(\vec{x})$ plus $\vec{u}_k$, the external influences, times $\mathbf{B}_k$, the matrix defining the influence on the system from the external values. In the estimation step the propagated values are corrected. First the Kalman gain $\mathbf{K}_k$ is computed with the measurement matrix $\mathbf{H}_k$ and the covariance matrix of the measurement noise $\mathbf{R}_k$ (1). Then the deviation of the system state $\Delta\vec{x}$ is computed with the propagated value, the Kalman gain and the difference out of the measurement deviation $\Delta\vec{z}_k$ and the propagated deviation of the system state (2). Afterwards (3), the error-covariance matrix is corrected with the unity matrix less the product of the Kalman gain times the measurement matrix. At last, the corrected system state is computed with the propagated system state and the estimated correction. Afterwards this cycle is re-executed for every time-step.

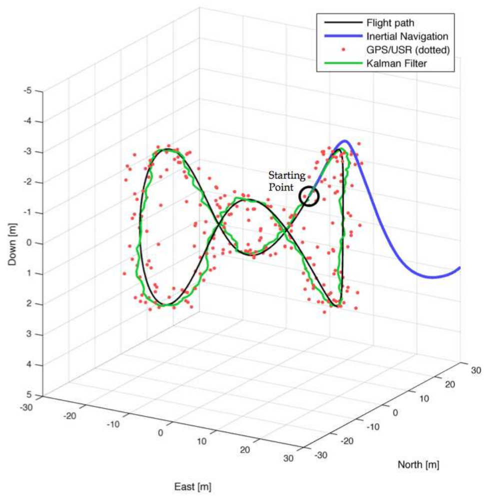

Fig. 4. Example result of the Kalman-filter [32]

With this Kalman filter implementation the trajectory of the helicopter can be reconstructed. In Fig. 4 the results for a generic example case are shown. In black a generic curve is given, which is distorted and analysed to achieve a generic measurement sensor output. Then, this 'output' is given into the filter loops to reconstruct the curve. In blue the result is shown if only the first loop is computed and all the information is only provided by the inertial measurement unit. Here the integrated noise leads to a fast growing big error. Therefore, the values of the USR and GPS (red dots) are fused to the data within the second loop. The green curve shows the very satisfying result. Tests with in-flight recorded data are currently underway.

3 NUMERICAL EXAMINATION

The numerical examination is divided in two parts. First the aerodynamics code FLOWer, which works out the flow field and all performance measures. Second is the structural dynamics section with the code CAMRAD II, which is employed to obtain the structural response for the force and moment computation of the CFD tool. Those two codes are iterated until a converged trim solution is obtained, which represents the experimental flight conditions. In the end the computed data can then be compared to the free flight test data for validation purposes of the CFD tool and the coupling with CAMRAD II.
With this toolchain it is possible to overcome the lack of validation data for new computational methods, for all flight cases which can be steered with a model helicopter. Although Reynolds and sometimes Mach scaling effects limit the direct transfer of physical flow phenomena to full scale, additional validation data is very valuable to explore new flight state territory. The few available full scale data will close the gap to a fully validated simulation system.

3.1 Aerodynamics

For the aerodynamic modelling of the helicopter the block structured finite volume Reynolds-averaged Navier-Stokes (RANS) CFD code FLOWer is used. For closure of the turbulence equations the Wilcox $k-\omega$ model[33] is implemented. To model the different helicopter components and their relative motion the Chimera technique was employed. A JST[34] stabilised central difference scheme leads to a second order accuracy in space discretisation. A dual time stepping, introduced by Jameson[35], is used to obtain second order accuracy in time. As a helicopter with moving and rotating grids is computed, the RANS solver has an arbitrary Lagrangian-Eulerian method implemented. In the present tool chain the CFD code is coupled with a flight mechanics code to realise a fluid structure coupling. As deformation of the blades and, therefore, the blade grids has to be computed, the geometric conservation law is employed. To improve and accelerate convergence, a multigrid algorithm and implicit residual smoothing are applied.

3.1.1 Setup

To obtain a numerical solution for the aerodynamics a grid setup was built up in Ref. 36 and was adapted for the use in the present examination. As mentioned, the Chimera technique is employed to handle relative motions of the several parts. In Fig. 5 the grid setup is shown. For better visibility the components are only depicted with edges, and parts of the background mesh are blanked. Around the aerodynamically interesting region of the helicopter the hanging grid nodes technique was employed, achieving a grid cell clustering in this region. All helicopter components were modelled with the exception of the skids and the blade brackets.

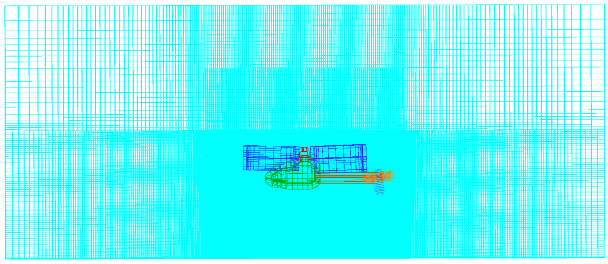

Fig. 5. Computational setup

Table 1 gives an overview of the grid components and their respective number of cells. In total the grid consists of about $69Mio$ grid cells in a block structured grid. The 3825 blocks are used to obtain a good parallelisation efficiency. At the helicopter surfaces and at the lower background mesh boundary a no slip wall was employed, to be able to compute the helicopter in ground effect. At these surfaces the mesh resolution is high enough to simulate the boundary layer. At the other boundaries of the background mesh a 'farfield' condition is applied.
The computations were performed at the Cray Hermit supercomputer at the high performance computing center in Stuttgart, on Dual Socket $2.3GHz$ AMD Interlagos processors.

Table 1. Grid components

mesh component	number of grid cells
background	$47,331,328$
fuselage	$12,324,864$
one main rotor blade	$3,075,584$
main rotor hub cap	$811,008$
one tail rotor blade	$751,104$
tail boom	$418,816$
vertical stabilizer	$208,896$
Total	$68,748,288$

3.2 Grid convergence study

This setup has to be studied with regard to the grid dependency. Therefore a grid convergence study according to Roache[37] was conducted.
Starting from a mesh quality commonly used at

IAG, this setup was refined and thinned out with a constant factor of 1.26 in each space dimension. Leading to three setups with 138, 69 and 40 Mio. grid cells, this resulted in an average refinement factor of $r_{32} = 1.2$ and $r_{21} = 1.26$ (coarse grid: index 3, medium grid: index 2 and fine grid: index 1). It was assured that the boundary layer thickness is kept constant and, furthermore, the height of the first cell was also constant, assuring a $y^+ \approx 1$ at the helicopter, the ground and the rotor blades. The aim was to evaluate discretisation errors via the grid convergence index (GCI).
In Tab. 2 the results of the evaluation are shown for different measures. As the main rotor possesses the major influence, the thrust C_T and torque C_{MT} coefficients of the main rotor and the lift C_L and pitching moment C_{MP} coefficients of the complete configuration are regarded. During the grid convergence study no trimming was performed, meaning that all setups are featuring the same flight condition, control settings and attitude angles. All GCI values were calculated using the safety factor of 1.25 used by Celik[38].

Table 2. Grid convergence study results

	$\Phi = C_T$ $[10^{-3}]$	$\Phi = C_{MT}$ $[10^{-4}]$	$\Phi = C_L$ $[10^{-3}]$	$\Phi = C_{MP}$ $[10^{-2}]$
Φ_3	2.567	−2.061	5.050	7.441
Φ_2	2.539	−1.982	4.998	6.084
Φ_1	2.533	−1.960	5.243	5.360
Φ_{ext}	2.532	−1.952	5.329	4.910
e_{ext}^{21}	0.058%	0.37%	1.62%	9.17%
GCI_{fine}^{21}	0.073%	0.46%	2.05%	10.5%
GCI_{refine}^{32}	0.37%	1.87%	0.67%	24.1%

The results of the grid convergence index values for C_T and C_{MT} show that the main rotor measures are converged and there is only a negligible influence of the mesh refinement from the coarse to the medium grid and nearly none from the medium to the fine grid. The measures of the complete setup show that there is still a notable grid influence. It is interesting that C_L seems to oscillate around the true solution. The pitching moment coefficient of the complete configuration still features a considerable grid dependency. However, as the most other coefficients show a satisfying behaviour, the medium refined grid setup is regarded as sufficiently accurate to compute the helicopter flight in ground proximity.
As shown, the integral features of the flow are modelled with an adequate precision, but as the wake characteristics are also of interest, they have to be examined either. Therefore, Fig. 6 gives a comparison of the wake features with λ_2-visualisations of the helicopter in forward flight from the starboard side. It is obvious that, the finer the grid, the better the resolution of the wake features, e.g. the blade tip vortices. Nevertheless, it can be seen that some features are not resolved properly in the coarse setup, whereas the gain of the fine setup compared to the medium resolution is not that big, to justify the double number of grid cells and, therefore, at least the double amount of CPU's or wall-clock time. Hence, the resolution of the flow features is regarded to be sufficient with the medium grid setup. Resulting out of the grid convergence study it was decided to use the medium setup for all further examinations.

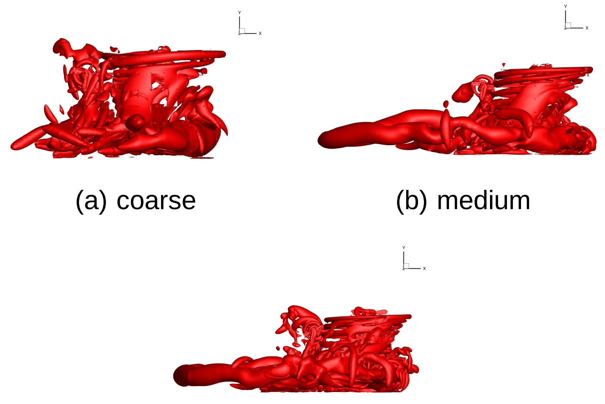
(a) coarse (b) medium (c) fine

Fig. 6. λ_2-visualisation of the helicopter setups with coarse, medium and fine grid resolution

3.3 Structural dynamics

The CAMRAD II code from Johnson Aeronautics[39] is used to compute the structural dynamics of the blades and the flight mechanics of the complete helicopter.
The forces on the body and the blades are in the first step computed with polars, the lifting line theory and the assumption of a high aspect ratio of the blades. The two-dimensional aerodynamics will be replaced by RANS CFD data in an iterative trim process (see chapter 3.4). The helicopter polars were generated in a wind tunnel campaign (see chapter 3.4.1), while the polars of the NACA0012 and NACA0013 were employed for the blades. Unsteadiness like dynamic stall or special conditions like gust and yawed winds could have been included via correction models. The wake can be represented either by analytical downwash-, prescribed- or free-wake-models.
CAMRAD II iterates with a Newton-Raphson algorithm the equilibrium condition of the acting forces. Here the aerodynamic forces on the body and the rotors and the centrifugal and gravitation/acceleration forces should reach a prescribed equilibrium condition.
The code is able to handle multibody dynamics and computes the exact rigid body movement of the he-

licopter components. To receive the elastic deformation of the components, the code needs, additionally to the computed loads, the elastic behaviour of the component. In this examination the main rotor blades are treated elastic, while the other components of the helicopter are regarded as rigid.
From the aerodynamic loads the structural deformation of the main rotor blades is computed. To achieve this, the code employs in the present implementation an Euler-Bernoulli beam model. This model represents the blades as a slender beam with isotropic material properties. The theory of the Euler-Bernoulli beam says that the undistorted cross-sections will stay undistorted during the deformation. Within this examination the beam is represented in CAMRAD II with second order accuracy and the code employs for the calculations the methodology of Ref. 40.

3.4 Trim procedure

From the experimental data, e.g. a phase with stationary forward flight and another one in hover may be chosen. In these states the velocity is known. Also, as the system is in a constant flight state, the sum of forces and moments on the complete helicopter must be equal to zero. To achieve this, the flight mechanics code predicts not only a structural deformation and control setting of the main rotor blades, but also a pedal setting and attitude angles of the helicopter. With this information, the CFD code computes the flow field and integrates the forces and moments out of the pressure distribution. Then these results are compared with the need of a force free helicopter. The flight mechanics tool predicts again all values, but with a correction employing the CFD forces and moments (Eq. 1). This information is again passed on to the CFD tool, which leads to an iterative process, in which the two-dimensional aerodynamic initial guess of the flight mechanics tool is replaced by the more accurate three-dimensional RANS solution. That way the deformation, blade articulation and helicopter movement is taken into account in the CFD computation, while a prescribed trim target (here force free flight) is achieved. This procedure is also known as free-flight or six-component trim, as the three main rotor control settings $\Theta_0, \Theta_s, \Theta_c$, the pedal setting and two helicopter attitude angles (here roll ϕ and pitch θ attitude) are trimmed. The third angle, here the yaw angle ψ, is prescribed, in this case equal to zero. This procedure was presented by Embacher[41] and Dietz and Dieterich[42], and is called 'loose complete helicopter coupling and trim'.
As a constant flight path is assumed, a periodicity of the loads is required, to obtain the controls for the next trim iteration (loose coupling). This may in some flight cases close to the ground (especially in manoeuvring flight) be difficult to achieve. If a non-periodic solution is obtained, a tight coupling approach must be used, in which the loads and deformation are exchanged and computed in every time step and not in a periodic flight phase, while the trim target is reached via a pilot model. In this work only the loose approach was used.
The loads, corrected with CFD data, are computed according to Ref. 42 with

$$\vec{F}^{n}_{eff} = \vec{F}^{n}_{2D} + \vec{F}^{n-1}_{3D} - \vec{F}^{n-1}_{2D}. \tag{1}$$

Here the effective loads which are used in CAMRAD II are composed out of the two-dimensional data of the actual 'n-th' trim iteration and a correction with the difference between the RANS CFD loads and the two-dimensional loads of the previous 'n-1-th' trim. With the time, the effective loads adapt to the three-dimensional RANS CFD loads. In the end a convergence is obtained when

$$\Delta\vec{F}^{n}_{2D} = \vec{F}^{n}_{2D} - \vec{F}^{n-1}_{2D} \rightarrow 0 \tag{2}$$

is achieved. Then the result of Eq.1 depends only on the three-dimensional CFD data. For a full derivation of the formulae see Ref. 42.

3.4.1 Wind tunnel

The body polars of the helicopter are necessary to obtain a valid start solution for the iteration process. During the trim loop those polars are subsequently replaced with values obtained by the aerodynamics code FLOWer. To achieve a fast and stable convergence, those polars should be as accurate as possible. Therefore, a wind tunnel campaign was conducted by Fahrenkamp[43]. In Fig. 7 the lift coefficient polar of the complete helicopter configuration without main rotor blades is depicted for the three velocities of $3m/s$ (blue), $6m/s$ (green) and $9m/s$ (red). These velocities were selected as the low speed forward flight in ground effect is of interest. At the lowest speed the quality of the wind tunnel flow is low. Therefore, and additionally because of flow separations at this low velocity, the polar is becoming unstable at high angles of attack (AoA; α), while the sideslip (β) influence is limited. One has to keep in mind that in the sideslip direction symmetry was assumed, therefore, only the positive angles were measured and then mirrored. Control measurements have shown, that although the helicopter is not fully symmetric, this assumption is feasible. With higher velocities the polar is much more stable, also at higher AoA values. Comparable results can be found in the other five force (drag and sideforce) and moment (moments around all body axes) polars. As the velocities were very small, it was often hard to minimize the error, because of the limited flow quality and small absolute forces at those low speeds. Nevertheless, the overall trend of the polars looks feasible, and the fact that the polar data will be replaced by CFD data during the trim process leads to the conclusion, that these polars will serve well for the implemented tool chain.

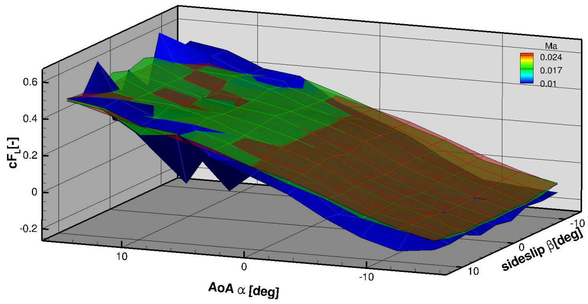

Fig. 7. Polar for the aerodynamic lift coefficient of the helicopter

Qualitative examination For a qualitative analysis it was important to see the overall behaviour of the aerodynamics around the helicopter, which was refurbished with a newly designed and built fuselage. Therefore, different velocities were examined to get a qualitative feeling of the behaviour of the flow. With regard to the blunt body of the helicopter, the flow is very satisfying. Different flow visualisation techniques were employed to visualise these findings. In Fig. 8 a laser light section on the upper front part of the fuselage is shown. The flow is visualised with oil smoke, which was injected upstream. It can be seen that the flow follows well along the body with nearly no disturbances. The flow underneath the body could not be detected very well, as there was the wind tunnel mounting system, which had a massive influence in this region. The conclusion in this sector of the fuselage, which could be drawn with respect to the mounting system, is that the flow follows astonishingly well along the shape of the hull (see Fig. 9).

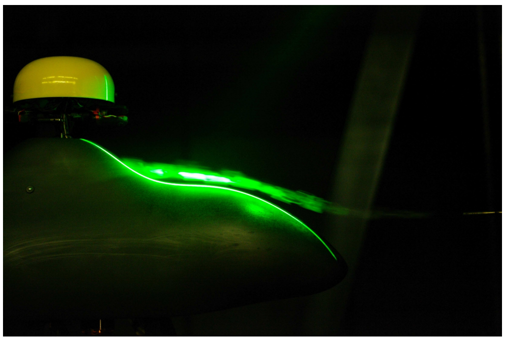

Fig. 8. Laser light section flow visualisation ($15 m/s$ and $\psi = 0°$, $\theta = 0°$, $\phi = 0°$) [43]

Figure 10 depicts the flow in the upper rear part of the helicopter. A huge blunt body separation zone is found. It can be seen that the flow follows the body and then separates at the sharp edge of the fuselage. Due to constraints in the way of attaching the fuselage

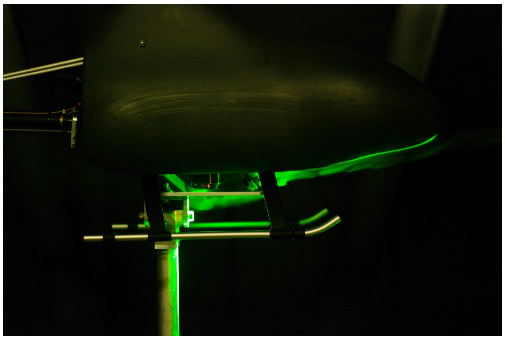

Fig. 9. Laser light section flow visualisation ($15 m/s$ and $\psi = 0°$, $\theta = 0°$, $\phi = 0°$) [43]

to the helicopter, this region can not be designed in another way. Therefore, a periodic separation motion of the flow and consequently oscillations of the forces on the body will be present, especially in fast forward flights. As in this examination the ground effect is of main interest, this will only have a minor impact on the measurements. Nevertheless, as the forces and moments at low flight speeds are small, the percentage of the fluctuations may be high.

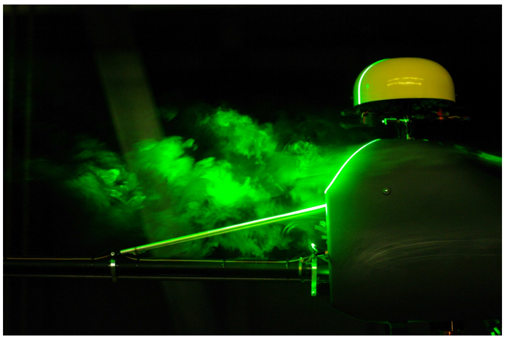

Fig. 10. Laser light section flow visualisation ($15 m/s$ and $\psi = 0°$, $\theta = 0°$, $\phi = 0°$) [43]

If a high AoA and sideslip angle is chosen, the flow still follows satisfactory along the body in the front part, but also shows considerable flow separation in the upper rear part, which will drastically increase the drag (see Fig. 11). This separation is much smaller at lower angles. When the rotor is turning, there will also be a major vertical flow component compared to a low forward flight velocity. Therefore, the helicopter body has to be a compromise between good flow quality at high and low flight speeds.

The qualitative analysis mirrors the result of the discussion of the polars. The overall behaviour is smooth and the flow quality is satisfying. At high angles or at low velocities the flow is becoming more unstable and the separation moves forward onto the

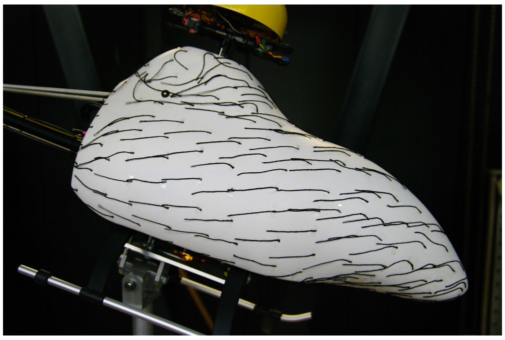

Fig. 11. Flow visualisation with woolen filaments ($15m/s$ and $\psi=-12°$, $\theta=-15°$, $\phi=-15°$) [43]

helicopter fuselage.

3.4.2 Structural modelling

The helicopter rigid body motion, attitude angles and the blade controls, as well as the dynamics of the main rotor blades and the trim of the complete system are, as already described, obtained via CAMRAD II. To acquire this information, the flight path, the velocity and the environment conditions are prescribed. The helicopter possesses one main rotor, where all controls and the elasticity are computed, and one tail rotor, at which the collective setting is coupled. The speed of revolution at the tail rotor is linked to the main rotor via the gear box ratio. The airframe polars serve as input as described earlier. As the modelling complexity is the biggest at the elastic main rotor blades, this procedure is described in the following.

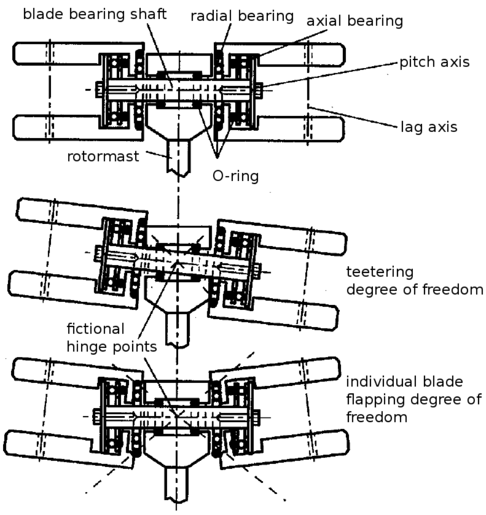

Fig. 12. Rotorhead (according to Ref. [1])

The blade model consists of 16 beam elements per blade with a higher resolution in the inboard section. The swashplate movement is modelled and the controls are introduced to the blade kinematics via the push rods. The flybarless rigid helicopter head features a combination of teeter and flap behaviour. This is modelled as in Fig. 12 shown with a teetering movement and an individual blade flapping. The lag hinge features a damping via the friction between the blade and the bracket. The pitch motion from the swashplate is inserted without a damper or spring. Ten fully dynamic modes per blade were used for coupling at the 26 aerodynamic panels. A uniform inflow model was chosen, as the computational costs could be reduced and as the aerodynamics will be replaced by the RANS CFD solution anyway. Figure 13 gives an impression about the motion and deformation of a rotor blade, as the initial blade position and the deformed blade, after the initial CAMRAD II trim, are shown.

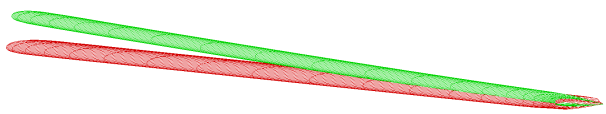

Fig. 13. Comparison between initial position (red) and deformed blade (green)

As the main rotor blade is modelled aerodynamically in CAMRAD with a NACA0013 and in FLOWer with the original geometry, which was extracted with a laser measurement system, a small error is present, which will also diminish with the coupling converging.

4 RESULTS, COMPARISON, AND VALIDATION

After the build up of the tool chain and modelling of the helicopter system, all components, systems and computational setups were tested separately until full functionality was achieved*. If a steady flight path is regarded, there are the following three possibilities to simulate the measured flight for comparison:

* At the moment the only component which is not fully operational is the Kalman-filter, as a special treatment of the inertial measurement data must be implemented, to reduce the influence of the rotor vibrations.

1. Prescribe the control settings and attitude angles of the experiment and compare the numerical forces and moments with the need of a force free steady flight. Furthermore, the performance measures may be checked for consistence.
2. Compute a free flight complete helicopter trim with the experimental height and speed, as well as the ambient conditions, and compare the controls and attitude of the helicopter with the measured ones.
3. Steer the experimental flight path and attitude with the help of a pilot model and compare the resulting controls.

At the moment the first two alternatives are implemented.

4.1 Flight test

After achieving operational readiness flight tests with steady flight states were performed. Table 3 gives an overview about the different testcases. The mean ambient temperature was $\approx 23°C$, while the mean ambient pressure was $\approx 95600Pa$. The height above mean sea level of the starting point was $417m$. Only very slow ambient winds from the portside were present during the flight. Hover flight was examined IGE and OGE, as well as forward flight IGE and OGE with different velocities. Further on, the flight Nr. 5 is examined.

Table 3. Flighttests

Nr.	Flight state	h/R [-]	mean flight speed $[m/s]$
1	Hover OGE	-	0.23
2	Hover IGE	0.554	0.14
3	Forward OGE	-	1.81
4	Forward IGE	0.72	1.49
5	Forward IGE	0.69	1.17

In Fig. 14 the pitch, flap and lag angle of the main rotor and the pitch angle of the tail rotor are depicted. A whole flight cycle can be seen, starting with the lift-off at about $time \approx 17s$, then the helicopter is stabilized in the air before forward flight is initiated. The forward flight measurement phase is indicated with black dashed lines and, it can be seen that during this phase a quite constant behaviour of the control settings is introduced. Afterwards the helicopter stops the forward flight and is starting a backward flight until the landing position is reached.
Figure 15 shows the measured height of the USR sensor and the GPS longitude and latitude, as well as

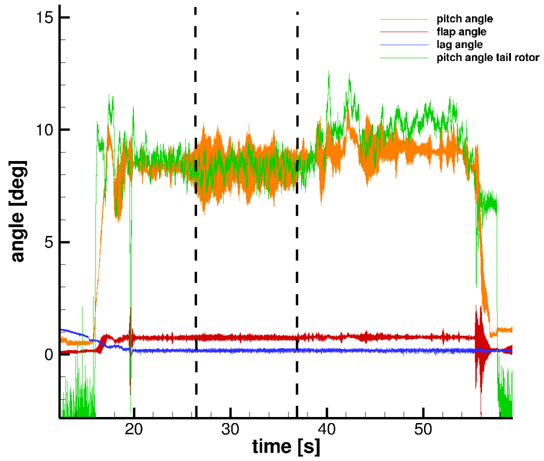

Fig. 14. Results of the Hall-sensors

the GPS measured heading. Again, the different flight phases may be detected. In these data it is clearly visible that the forward flight phase is a stationary forward flight with a nearly constant height, heading and speed.

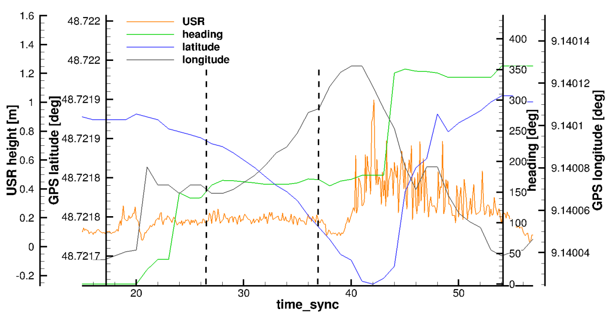

Fig. 15. Results GPS and USR sensor

JLOG2 data is given in Fig. 16. In green the throttle setting is shown, while the grey curve gives the angular rate of the main rotor. The orange curve depicts the voltage of the batteries and the red one the current through the motor. The blue curve illustrates the power consumption of the motor. During the whole flight these measures are quite constant and reinforce the assumption of a steady flight state.

4.2 Computational results

4.2.1 Uncoupled computation

The first simulation possibility was selected to start the computational validation. The mean collective pitch of the main and tail rotor were extracted from

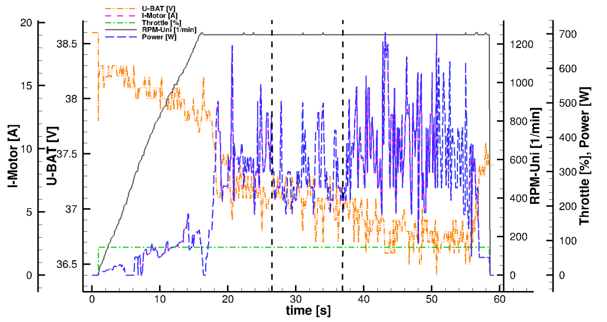

Fig. 16. Logged data of the JLOG2

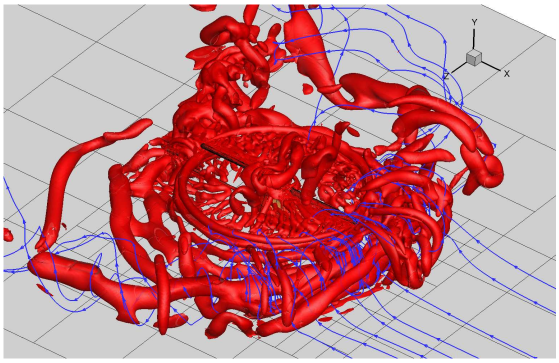

Fig. 17. λ_2-visualisation of the flow field after 19 revolutions

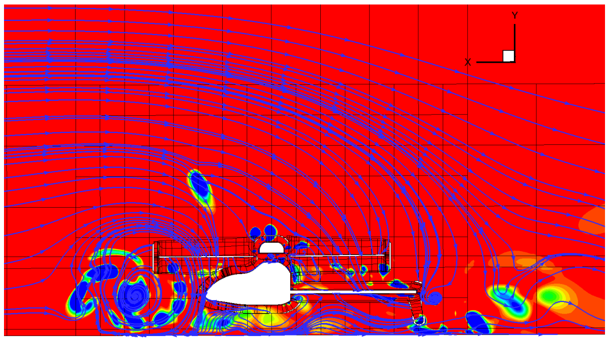

Fig. 18. Streamtraces and λ_2 contour on vertical slice after 19 revolutions

the experiment. Further on, the longitudinal and lateral setting of the main rotor were determined with a curve fit from the free flight measurement. As this computation is not trimmed with CAMRAD II, the controls were set accordingly to the measurements and, therefore, the computation should lead to a force and moment free helicopter in constant forward flight. As the Kalman-filter is not yet fully functional, the pitch and roll values of the fuselage were estimated from an initial CAMRAD II trim.

It is important that a converged flow field in ground effect flight is achieved. Here 19 revolutions were more than sufficient to gain a satisfactory convergence of the numerics and the flow physics. Furthermore, the last 2 revolutions were taken into account to average the force and moment measures. Table 4 gives an overview of the total aerodynamic forces and moments on the helicopter. It is shown that on the helicopter a propulsive force F_x, a lifting force F_y and a side force F_z are acting. The CFD power consumption of both rotors is $P_{aero} = 351W$.

The Figures 17 and 18 show a λ_2-visualisation of the flow field after the 19 revolutions. A distinct horseshoe vortex lies in front of the helicopter forming a recirculating fluid flow. The streamtraces are indicating the fluid flow. The fluid trapped in the vortex in front of the helicopter can be seen clearly and also the helical fluid flow along the horseshoe vortex is present. In this examination vortices moving upwards along the horseshoe vortex and recirculating into the rotor disk area can be found, especially in the front section. This behaviour was also present in the examination of Ref. 29 and may indicate one of the driving aerodynamic mechanisms for brown-out. These upward moving vortices may contain material and transport it high into the flow field. On the port side of the helicopter the horseshoe vortex is disturbed from the tail rotor wake. Fragments are blown up high into the flow field. The dissipation of the horseshoe vortex, when exiting the refined mesh region in the back, is also clearly visible. The vortices of the simulated hub cap merge with the inner vortices of the blades, in the center of the rotor disk.

Table 4. Results of the uncoupled computation

$F_x[N]$	$F_y[N]$	$F_z[N]$
-0.21	37.4	5.7
$M_x[N/m]$	$M_y[N/m]$	$M_z[N/m]$
-1.7	2.82	-0.08

4.2.2 Coupled computation

The coupled complete helicopter simulation was then performed, to show the applicability of the implemented tool chain. Fig. 19 show the control settings during the different trim iterations. Obviously a convergence was achieved in the collective pitch setting. Nevertheless, the cyclic settings are not converged perfectly yet, here some more trim iterations are needed. IGE the forces on the helicopter and the blades are assumed to be very unsteady, depending on the flight state and the proximity to the ground. This is due to the unsteady effects, e.g. vortex reflections at the ground and recirculation effects. Consequently, a long time period has to be computed to assure a sufficiently converged flow field.

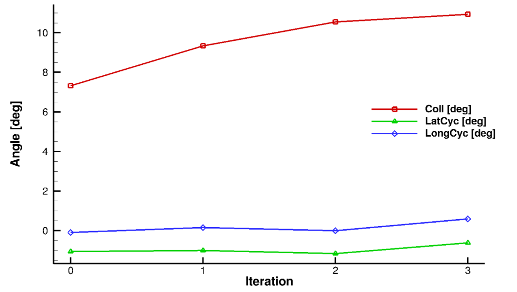

Fig. 19. Control settings during the trim process

The rotor forces of the last $180°$ in the second trim step are depicted in Fig. 20. It can be seen that the longitudinal and lateral forces are about zero and, furthermore, that the thrust features a considerable oscillation. A FFT, shown with the red line, depicts the frequency content of the thrust development. Oscillations of up to 60 times per revolution are present and lead to the oscillatory content. This is the proof for the assumed unsteadiness described before.

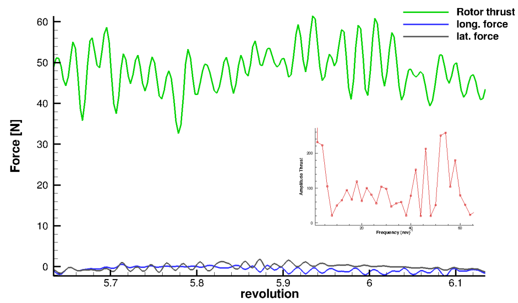

Fig. 20. Main rotor forces of the last 180deg of trim 2

4.3 Comparison and validation

4.3.1 Uncoupled computation

To counteract the weight of the helicopter, the aerodynamic forces of the uncoupled simulations should be around $F_x \approx 0N$, $F_z \approx 2.5N$ and $F_y \approx 49N$, while the moments should be $\approx 0Nm$. From Tab. 4 it may be seen that the moments are quite small, but, especially M_y, not equal to zero. The forces in x and z direction match well with the weight, while F_y is too small. Therefore, a coupled simulation is needed to compute the exact same flow topology. The power may be compared to the measured one, if the losses of the motor and the gear are taken into account. Therefore, calibration runs were performed in advance. These lead to an electric loss of $P_\Omega = 1.5W$, a motor loss of $P_M = 77W$ and a gear friction loss of $P_G = 19.3W$. In total, the power consumption of the motor will be $P_{total} = P_{aero} + P_\Omega + P_M + P_G = 448.8W$. When compared to the experimental value of $P_{exp} = 295W$ it is seen that CFD overestimates the experimental measurement.
The comparison of the wake characteristics may be done with the normalised advance ratio, defined by Curtiss et al.[4]

$$\mu^\star = \mu * \sqrt{\frac{2}{c_T}} = \frac{v_\infty cos(\alpha)}{\Omega R} * \sqrt{\frac{2}{\frac{F_T}{\rho A (\Omega R)^2}}}, \quad (3)$$

leading to $\mu^\star_{exp} \approx 0.3$ and $\mu^\star_{CFD} \approx 0.35$. With the height to Radius ratio of $h/R = 0.69$ it can be stated, that both, the experiment and the uncoupled computation, are in the transition phase to the state of recirculation, which coincides well with the visualisation in Fig. 17.

4.3.2 Coupled computation

A higher collective setting as in the experiment was reached, which was expected after the findings in the uncoupled simulation run. As it can be expected the power consumption is now even higher than in the uncoupled run, as the collective setting is increased, leading to $P_{aero} = 450W$. But, it is now guaranteed, that the same flow field and same normalised advance ration is considered.

5 SUMMARY AND OUTLOOK

Summary To overcome the lack of test data for free flights of helicopters, a model based system was set up, equipped and tested. Furthermore, a computational setup was built up and implemented in the tool chain, modelling a CFD/CSD coupled complete helicopter with elastic main rotor blades in a free flight trim. With this new process it is now possible to validate new models or methods, like the higher order WENO schemes in FLOWer, or other flight regimes like ground effect, with respect to the model scale.
It is now possible to perform all necessary flight manoeuvres with data logging. Different free flight tests were performed and analysed. Unfortunately the accelerometer and gyroscope output is afflicted with a lot of noise from the rotor vibrations.
The uncoupled computation shows that the CFD code underestimates the thrust force, while overestimating the power consumption. The flow regime is reproduced well and also the wake effects match well with the literature. The coupled computation is capable to capture the qualitatively same flow field as in the experiment. Furthermore, the helicopter is computed force free. A high oscillatory content is found in the thrust development of the main rotor. The power consumption is highly overestimated.

Outlook Especially the Kalman-filter is in the current focus, as the data of the gyroscope and accelerometer feature a considerable influence of the main rotor vibrations, and here a filtering must be incorporated.
If needed, the experimental test equipment can be extended with strain gauges at the main rotor blades, as the measurement system is already prepared to log this data as well.
After the full operationality of the Kalman-filter is reached, the already measured data will be post-processed and the coupled computation may be compared better. In future, further measurements, especially in manoeuvre flight in ground effect, will be conducted and validated. Also the higher order WENO scheme will be incorporated in ground effect computations. Furthermore, the power prediction capability has to be improved.

Copyright Statement

REFERENCES

[1] Fischer, A., *Untersuchung zur Aeromechanik eines flugfähigen Hubschraubermodells*, Ph.D. thesis, University of Stuttgart, Faculty of Aerospace Engineering, Institute of Aerodynamics and Gasdynamics, 2004.

[2] Kroll, N., Eisfeld, B., and Bleeke, H., "The Navier-Stokes code FLOWer," *Notes on Numerical Fluid Mechanics*, 1999, pp. 58–71.

[3] Light, J. S., "Tip vortex geometry of a hovering helicopter rotor in ground effect," Proceedings of the American Helicopter Society, 45th Annual Forum, Boston, MA, 1989.

[4] Curtiss, H. C., Sun, M., Putman, W. F., and Hanker Jr., W. J., "Rotor aerodynamics in ground effect at low advance ratios," Proceedings of the American Helicopter Society, 37th Annual Forum, New Orleans, LA, May 1981.

[5] Nathan, N. D. and Green, R. B., "The flow around a model helicopter main rotor in ground effect," *Experiments in Fluids*, Vol. 52, 2012, pp. 151–166.

[6] Betz, A., "The ground effect on lifting propellers," *Zeitschrift für angewandte Mathematik und Mechanik*, Vol. 17, (2), April 1937.

[7] Heyson, H. H., "Ground effect for lifting rotors in forward flight," NASA TN D-234, NASA, 1960.

[8] Fradenburgh, E. A., "The helicopter and the ground effect machine," Symposium on Ground Effect Phenomena, Princeton, NJ, October 1959.

[9] Hayden, J. S., "The effect of the ground on helicopter hovering power required," Proceedings of the American Helicopter Society, 32nd Annual Forum, Washington, D.C., 1976.

[10] Zbrozek, J., "Ground effect on the lifting rotor," R.A.E. Technical Note No. Aero. 1903 2347, Aeronautical Research Council, 1947.

[11] Cheeseman, I. C. and Bennett, W. E., "The effect of the ground on a helicopter rotor in forward flight," A.A.E.E. Report Rey./288 3021, Aeronautical Research Council, 1955.

[12] Sheridan, P. F. and Wiesner, W., "Aerodynamics of helicopter flight near the ground," Proceedings of the American Helicopter Society, 33th Annual Forum, Washington, D.C., May 1977.

[13] Lee, T. E., Leishman, J. G., and Ramasamy, M., "Fluid dynamics of interacting blade tip vortices with a ground plane," Proceedings of the American Helicopter Society, 64th Annual Forum, Montral, Canada, May 2008.

[14] Saijo, T., Ganesh, B., Huang, A., and Komerath, N. M., "Development of unsteadiness in a rotor wake in ground effect," AIAA 21st Applied Aeromdynamics Conference, Orlando, FL, June 2003.

[15] Xin, H., Prasad, J., and Peters, D. A., "An analysis of partial ground effect on the aerodynamics of a helicopter rotor," AIAA 38th Aerospace Sciences Meeting and Exhibit, Reno, NV, January 2000.

[16] Bhattacharyya, S. and Conlisk, A., "The structure of the rotor wake in ground effect," AIAA 41th Aerospace Sciences Meeting and Exhibit, Reno, NV, January 2003.

[17] Griffiths, D. A., Ananthan, S., and Leishman, J. G., "Predictions of rotor performance in ground effect using a free-vortex wake model," Proceedings of the American Helicopter Society, 58th Annual Forum, Montral, Canada, May 2005.

[18] D'Andrea, A., "Unsteady numerical simulations of helicopters and tiltrotors operating in sandy-desert environment," Proceedings of the American Helicopter Society Specialist's Conference on Aeromechanics, San Francisco, CA, January 2010.

[19] Moulton, M. A., O'Malley, J. A., and Rajagopalan, R. G., "Rotorwash prediction using an applied computational fluid dynamics tool," Proceedings of the American Helicopter Society, 60th Annual Forum, Baltimore, MD, June 2004.

[20] Kang, N. and Sun, M., "Simulated flowfields in near-ground operation of single- and twin-rotor configurations," *Journal of Aircraft*, Vol. 37, (2), March-April 2000, pp. 214–220.

[21] Phillips, C. and Brown, R. E., “Eulerian simulation of the fluid dynamics of helicopter brownout,” Proceedings of the American Helicopter Society, 64th Annual Forum, Montral, Canada, May 2008.

[22] Brown, R. E. and Whitehouse, G. R., “Modelling rotor wakes in ground effect,” *Journal of the American Helicopter Society*, Vol. 49, (3), 2004, pp. 238–249.

[23] Kalra, T. S., Lakshminarayan, V. K., and Baeder, J. D., “CFD validation of micro hovering rotor in ground effect,” Proceedings of the American Helicopter Society, 66th Annual Forum, Phoenix, AZ, May 2010.

[24] Nathan, N. D., *The rotor wake in ground effect and its investigation in a wind tunnel*, Ph.D. thesis, University of Glasgow, Faculty of Engineering, Department of Aerospace Engineering, 2010.

[25] Pulla, D. P., *A study of helicopter aerodynamics in ground effect*, Ph.D. thesis, The Ohio State University, 2006.

[26] Ganesh, B., *Unsteady aerodynamics of rotorcraft at low advance ratios in ground effect*, Ph.D. thesis, Georgia Institute of Technology, School of Aerospace Engineering, 2006.

[27] Schmid, S., Lutz, T., and Krämer, E., “Impact of ground modelling approaches on the prediction of ground effect aerodynamics,” *Engineering Applications of Computational Fluid Mechanics*, Vol. 3, (3), 2009, pp. 419–429.

[28] Kutz, B. M., Bensing, F., Keßler, M., and Krämer, E., “CFD calculation of a helicopter rotor hovering in ground effect,” *Notes on numerical fluid mechanics and multidisciplinary design*, Vol. 121, Dillmann, A. and Heller, G. and Kreplin, H-P. and Nitsche, W. and Peltzer, I., eds., 2013, pp. 297–304.

[29] Kutz, B. M., Kowarsch, U., Keßler, M., and Krämer, E., “Numerical investigation of helicopter rotors in ground effect,” Paper AIAA-2012-2913, 30th AIAA Applied Aerodynamics Conference, New Orleans, LA, 2012.

[30] Kutz, B. M., Keßler, M., and Krämer, E., “Experimental and numerical examination of a helicopter hovering in ground effect,” *CEAS Aeronautical Journal*, 2013. doi: 10.1007/s13272-013-0084-x

[31] Kutz, B. M., Braun, A., Keßler, M., and Krämer, E., “Free flight measurement environment for model helicopters,” 62 Deutscher Luft- und Raumfahrtkongress, Stuttgart, 2013.

[32] Braun, A., *Aufbau eines Kalmanfilters zur Bestimmung der Flugtrajektorie der Messplattform DAEDALUS*, Master’s thesis, University of Stuttgart, Faculty of Aerospace Engineering and Geodesy, Institute of Aerodynamics and Gasdynamics, March 2013.

[33] Wilcox, D. C., “Reassessment of the scale-determining equation for advanced turbulence models,” *AIAA Journal*, Vol. 26, November 1988, pp. 1299–1310.

[34] Jameson, A., Schmidt, W., and Turkel, E., “Numerical solutions of the Euler equations by finite volume methods using Runge-Kutta time-stepping schemes,” AIAA 14th Fluid and Plasma Dynamic Conference, Palo Alto, CA, 1981.

[35] Jameson, A., “Time dependent calculations using multigrid, with applications to unsteady flows past airfoils and wings,” AIAA 10th Computational Fluid Dynamics Conference, Honolulu, HI, 1991.

[36] Hofmann, T., *Modellierung der Messplattform DAEDALUS mit Hilfe der Software GRIDGEN und FLOWer*, Bachelorarbeit, University of Stuttgart, Faculty of Aerospace Engineering and Geodesy, Institute of Aerodynamics and Gasdynamics, October 2012.

[37] Roache, P. J., “Quantification of uncertainty in computational fluid dynamics,” *Annual Review of Fluid Mechanics*, Vol. 29, 1997, pp. 123–160.

[38] Celik, I. B., Ghia, U., Roache, P. J., Freitas, C. J., Coleman, H., and Raad, P. E., “Procedure for estimation and reporting of uncertainty due to discretization in CFD applications,” *Journal of Fluid Engineering*, Vol. 130, 2008.

[39] Johnson, W., *CAMRAD II Comprehensive analytical model of rotorcraft aerodynamics and dynamics*, fourth edition, 2009.

[40] Hodges, D. and Dowell, E., “Nonlinear Equations of Motion for the Elastic Bending and Torsion of Twisted Nonuniform Rotor Blades,” NASA TN D-7818, NASA, 1974.

[41] Embacher, M., Keßler, M., Dietz, M., and Krämer, E., “Coupled CFD-Simulation of a Helicopter in Free-Flight Trim,” Proceedings of the American Helicopter Society, 66th Annual Forum, Phoenix, Az, May 2010.

[42] Dietz, M. and Dieterich, O., “Towards Increased Industrial Application of Rotor Aeroelastic CFD,” Proceedings of the 35th European Rotorcraft Forum, Hamburg, Germany, September 2009.

[43] Fahrenkamp, J., *Vermessung der Messplattform DAEDALUS im mittleren Windkanal zur Gewinnung von Rumpfpolaren*, Bachelorarbeit, University of Stuttgart, Faculty of Aerospace Engineering and Geodesy, Institute of Aerodynamics and Gasdynamics, October 2012.